Supporting Information

Near Surface Nucleation and Particle Mediated Growth of Colloidal Au Nanocrystals

Yingwen Cheng[1], Jinhui Tao[2], Guomin Zhu[2,3], Jennifer A. Soltis[2],

Benjamin A. Legg[2], Elias Nakouzi[2], James J. De Yoreo[2,3], Maria L. Sushko[2], Jun Liu[1]

[1]Energy Processes & Materials Division, Pacific Northwest National Laboratory, Richland, WA 99352

[2]Physical Sciences Division, Pacific Northwest National Laboratory, Richland WA 99352

[3]Department of Materials Science and Engineering, University of Washington, Seattle, WA 98185

Experimental Section

Materials.: Tetrachloroauric acid ($HAuCl_4$), trisodium citrate ($Na_3C_6H_5O_7$), sodium hydroxide (NaOH), sodium nitrate ($NaNO_3$) and nitric acid (HNO_3) were all of analytical grade and were purchased from Sigma-Aldrich. Ultrapure water with resistivity higher than 18 MΩ/cm generated with an EMD Millipore Direct-Q 3-R ultrapure water purification system was used for preparation of aqueous solutions in all experiments.

Synthesis: The colloidal gold nanoparticle seeds were prepared by following the Turkevich method.[1] In a typical procedure, 100 ml aqueous solution of $HAuCl_4$ (0.2 mM) was put into a 250 ml flask and was heated to boiling under mechanical stirring, then 0.5 ml of trisodium citrate solution (0.2 M) was added. After about one minute a very faint greyish-pink tone developed and gradually darkened over a period of about two minutes. The reaction was run until the color became deep wine red (typically 10 min) and then was removed from heat and allowed to cool.

The ultra violet-visible (UV-Vis) absorption spectra (Figure S1) show a characteristic peak at ~525 nm, and analysis of *ex situ* TEM images revealed a typical spherical morphology of the as-synthesized seed nanocrystals. The resulting seed diameter of 17.0 ± 0.4 nm agrees well with previously reported data.[1-2] The nanocrystals exhibited high colloidal stability, which has been previously attributed to electrostatic stabilization by adsorbed citric anions.[3-4]

The seeded growth experiment was performed by adding 0.1 ml of 20 mM $HAuCl_4$ and 0.2 ml of 20 mM Na_3Cit solution to 10 ml of the seed solution and solution pH was 6 – 6.5. All seeded growth experiments were performed at room temperature (~ 20°C) and generally took several hours to finish. Samples were periodically collected for *in situ* and *ex situ* characterizations.

Characterization:

UV-Vis absorption. UV-Vis absorption spectra were recorded on a Shimadzu UV-3600 UV-VIS-NIR spectrophotometer.

TEM experiments. All TEM images were acquired using an FEI Tecnai G^2 Twin microscope operated at 200 kV and equipped with an Eagle camera (FEI). *Ex situ* samples were prepared by placing a drop of the colloidal solution onto a Formvar-coated copper grid. *In situ* liquid cell experiments were performed in a Hummingbird liquid cell holder using silicon nitride chips with 100 nm spacer, and typical electron dose was 134 $e^-/Å^2$•s. *Cryo* TEM samples were prepared by placing 3 µL of colloidal solution onto a copper TEM grid coated with lacey carbon, blotting the grid with filter paper, and plunging it into liquid ethane. The vitrified specimens were then handled and stored under liquid nitrogen and imaged in a Gatan 626 *cryo* TEM holder at -176 °C.

To analyze the *in situ* TEM data, we first used the MIPAR software to locate the Au particles by passing the images through median and basic threshold filters. Subsequently, an in-house MATLAB routine was used to locate the contour pixels of each particle, measure the distances between contour points belonging to different particles, and hence determining the minimum separation between any two particles. The analysis allows us to measure the particle size and separation as a function of time.

Beam effects on nucleation. Detailed *in situ* TEM studies on the effect of the beam on noble metal nucleation show that the rate of nucleation increases with electron dose due to the production of hydrated electrons (e^-_{aq}), which act as a reductant (See for example,

Woehl et al.[5]). The beam also effects the collapse of metal nanoparticle suspensions, because the charged radiolysis products play the role of background electrolytes that screen electrostatic repulsion and permits the van der Waals attractive force to dominate.[6] In all of those studies, the behavior of the particles is essentially as expected, but the electron beam accelerates the processes. None-the-less, for any given system, ensuring that the pathway and outcome are not determined by the beam, but rather only the rate is affected, is critical. There are two common ways to do this. The first is to collect *ex situ* and *cryo* TEM images to see whether the morphology produced during *in situ* TEM experiments is manifest. The corresponding data are presented in Figures 2 and 5. In fact, it is from these experiments that we first observed evidence for particle aggregation and the formation of necks. From those observations, we hypothesized the mechanism then observed *in situ*. The second is to blank the beam, as discussed on p. 3 in the main text:

The theoretical estimates suggest that beam induced heating in Au nanoparticle solutions is responsible for local temperature change of 0.2 – 0.7 degrees for dose rates 100 – 150 $e^-/Å^2$•s (SI to ref.[7]). We used mild dose rate of 134 $e^-/Å^2$•s, to minimize beam effects on nucleation and growth. Another effect of electron irradiation during TEM experiment in aqueous solutions is water radiolysis, which induces the reduction of solution metal species and affects the kinetics of crystal growth.[5, 8-9] Previous studies point to beam induced change in the growth kinetics, which was found to be surface reaction limited at low beam current and diffusion limited at high dose rates and leads to different crystal morfphologies.[5, 9] However, there is no evidence that dose rate affects nucleation pathways, which is the focus of the present study. To confirm that the key *in situ* TEM observations are not affected by beam-induced solution radiolysis or heating, we used complementary experimental methods, which do not rely on electron beam irradiation of the sample.

AFM characterization. The growth behavior of Au nanocrystal seeds was also examined using *in situ* AFM (Digital Instruments J scanner, Nanoscope 8, Bruker). Hybrid probes consisting of silicon tips on silicon nitride cantilevers (HYDRA triangular lever, k=0.088 N/m, tip radius <10 nm; resonance frequency 75 kHz in air; Applied Nanostructures, Inc, www.appnano.com) were used. The tapping mode was adopted to minimize the force between the seeds and the AFM tip.[10]

The seed particles were deposited on a poly-L-lysine modified mica substrate, which was immediately transferred to the AFM fluid cell. A muscovite mica disc (diameter 9.9 mm, Ted Pella, Inc) was freshly cleaved and used as a supporting surface. A poly-L-lysine solution (0.1% w/v, Ted Pella, Inc) was placed onto the mica surface for 5 min, and was then thoroughly rinsed with water and dried by a stream of nitrogen gas. The substrates were prepared by placing a drop of gold nanoparticles colloidal solution on poly-L-lysine modified mica surface, and left in contact for 30 min. Unabsorbed particles were then rinsed away with water and the substrate was transferred to a AFM fluid cell. A growth solution consisting aqueous 0.2mM $HAuCl_4$ and 1.4mM Na_3Cit (without any primary seeds) adjusted to desired pH values was injected to the fluid cell. All of the growth solutions were filtered through filter membranes (pore size 0.22 μm, PVDF, AcroDisc LC, PALL) prior to use. All the AFM imaging was performed at room temperature under static conditions (without fluid flowing). The evolution of the seed crystals was continuously monitored over the course of several hours.

Although lysine functionalized surface will generate an electric field, that may influence distribution and dynamics of charged and polarizable solution species, the lysine effect is expected to be local due to ionic screening. In all reaction conditions the ionic strength is between 1.5 mM and 3.2 mM at different pHs and the corresponding Debye screening length is in the range of 5-8 nm, while the height of the gold nanoparticle is in the range of 15-20 nm, as determined from our growth kinetic curves and form size distribution analysis from TEM images. Given that the height of gold nanoparticle is more than 2 time larger than the Debye length, and that in AFM experiments the changes in nanoparticle height above the substrate are monitored, the screened electric field of the substrate should only have a very limited effect on the distribution of solution species and nucleation and growth process over 15 nm above the substrate. The influence of lysine on nucleation of new particles may be expected close to the substrate. However, those particles do not contribute to the growth of the seeds or modify the seeded growth pathway.

DFT calculations: The focus of the theoretical simulations was on the understanding the thermodynamic driving forces for non-classical nucleation and growth pathway. To achieve this goal, we used a DFT-based atomistic-to-mesoscale approach we developed.[11-12]

Plane wave DFT simulations were used to determine the binding energy and configuration of citrate and auric acid species on Au surface. Simulations were performed using DFT with PBE exchange-correlation functional and projector augmented wave potentials, as implemented in the VASP code. The plane-wave basis with a 500 eV cutoff and a $2 \times 2 \times 2$ Monkhorst–Pack grid were used. Au (111) surface was modelled as a 144-atom slab and a 15 Å vacuum gap was used to avoid interactions between the slabs.

The details of the classical density functional theory (cDFT) formulation used in this work were described in detail elsewhere.[11] The aqueous salt solution was modeled as a dielectric medium with ε = 78.5, consisting of discrete charged spherical particles representing ions, and neutral spherical particles representing water molecules. The concentration of spherical "water molecules" was 55.5 M, chosen to model experimental water density. We used experimental crystalline ionic diameters for mobile ions equal to 0.65 nm for citrate species and 0.67 nm for auric acid species. Simulations were performed at pH 6 and the ion charges reflected the dominant species at this pH and were equal to -2 for citrate species, -1 for auric acid, and 0 for water.[13] Short-range interactions were treated explicitly. Interactions of citric and auric anions with Au (111) surface were calculated using plane-wave DFT (Figure S6) and the adsorption energies were found to be equal to -1.252 eV and -0.78 eV, respectively. Note, citrate configuration used in these calculations corresponds to citrate adsorption configuration in aqueous solution[14] as opposed to that in vacuum.[15] Experimental enthalpies of hydration were used for short-range inter-actions of citric and auric ions with water. Citric anion-water interactions are attractive with hydration enthalpy equal to ΔH_{Cit2-}=-1.0 eV,[14] while auric anion-water interactions are repulsive with ΔH_{AuX-}=+0.65 eV.[16]

Informed by plane-wave DFT, cDFT simulations account only for *average* chemical interactions between ion and solvent species with the surface and between the species, e.g. solvation interactions, which limits the applicability of the approach to interparticle separations of no smaller than 0.5 nm. However, as reported in our previous publications, the accuracy of our classical DFT model in calculating thermodynamic properties of electrolyte solutions, e.g. ion activity in a wide concentration range, and ion distribution at complex interfaces exceeds that of all-atom molecular dynamics with standard force-fields and the calculated results are in close agreement with state-of-the-art experimental data,[17-18] rendering the methodology adequate for the task.

Monitoring Au nanoparticle growth without seed

The study of Au nanoparticle growth without seeds was performed as follows. 100 ml aqueous solution of $HAuCl_4$ (0.2 mM) was put into a 250 ml flask and was heated to boiling under mechanical stirring. Then 0.5 ml of trisodium citrate solution (0.2 M) was added. After about one minute a faint greyish-pink color developed and gradually darkened over a period of about two minutes. At this stage, the growth solution consists of agglomerates of particles few nanometers in size (Figure S7). The evolution of these agglomerates was closely monitored. The growth solution was immediately quenched by using an ice bath and subsequent experiments were performed at room temperature following the same protocol as that for seeded growth experiments. The time zero was defined as the time when the sample was cooled to room temperature. Figure S7 present a set of typical TEM images collected at different time. Together with Figure 6, these images outline structure-morphology evolution of agglomerates.

Movies S1 – S2. *In situ* TEM movies of seeded growth of Au nanoparticles under neutral growth condition (pH 6.5). 1 frame per second.

Movie S3. Analysis of *in situ TEM* movie showing the detection of Au nanoparticles using MIPAR and MATLAB.

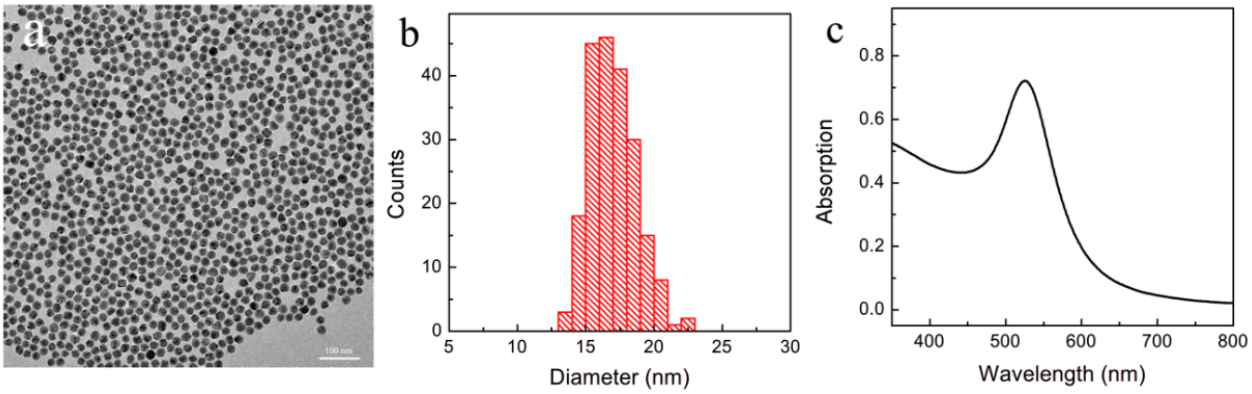

Figure S1. *Characterization of gold seed nanoparticles synthesized by reacting 0.2 mM $HAuCl_4$ with 1.0 mM Na_3Cit in 100 ml water under boiling for 10 min. a) Representative TEM image and b) the corresponding histogram that shows the size distribution; c) UV vis absorption spectrum that shows characteristic absorption peak at 530 nm. The scale bar in (a) is 100 nm.*

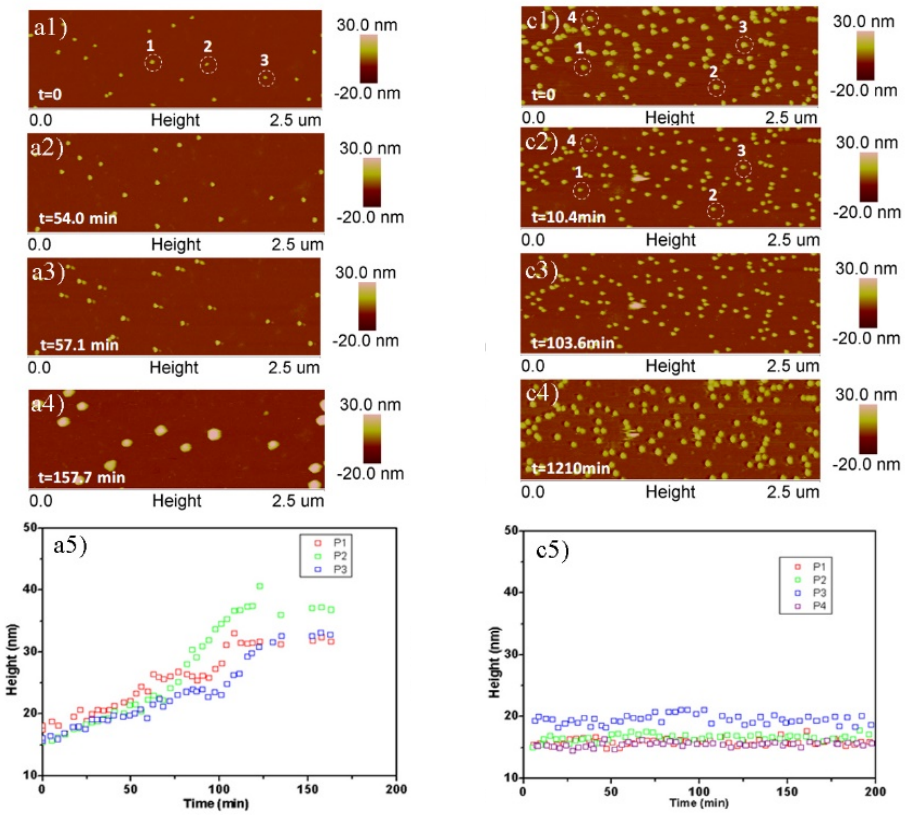

Figure S2. *In situ atomic force microscopy images of seeded growth of gold nanoparticles at pH 3.4 (a-e) and 11.2 (f-j). Zero-time point corresponds to the growth solution injection time. (a-d) sequential AFM images collected at different time as noted and (e) the corresponding particle height evolution of the circled particles as a function of reaction time; (f) temporal evolution of UV-Vis spectrum that shows increases*

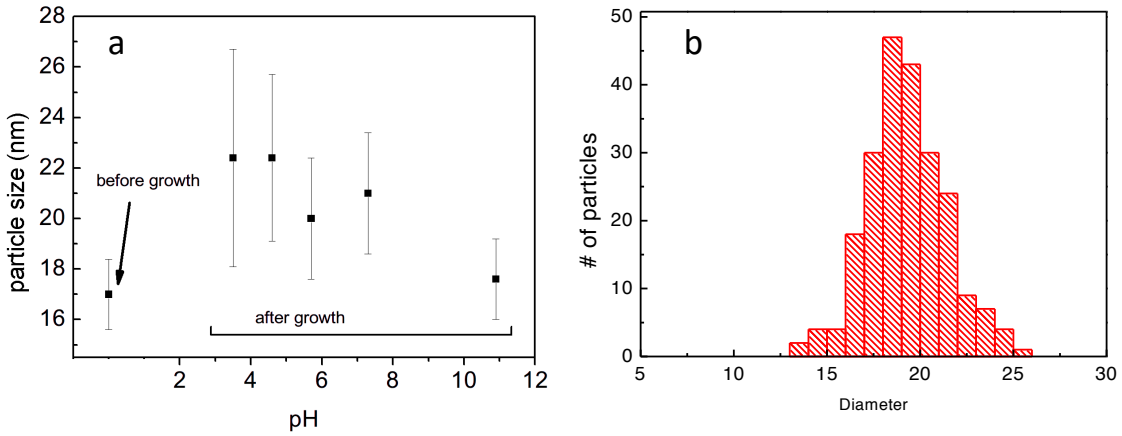

***Figure S3**. Particle size distribution after growth for a) 1 week at different pH, and b) after 7 hours at pH 6.5.*

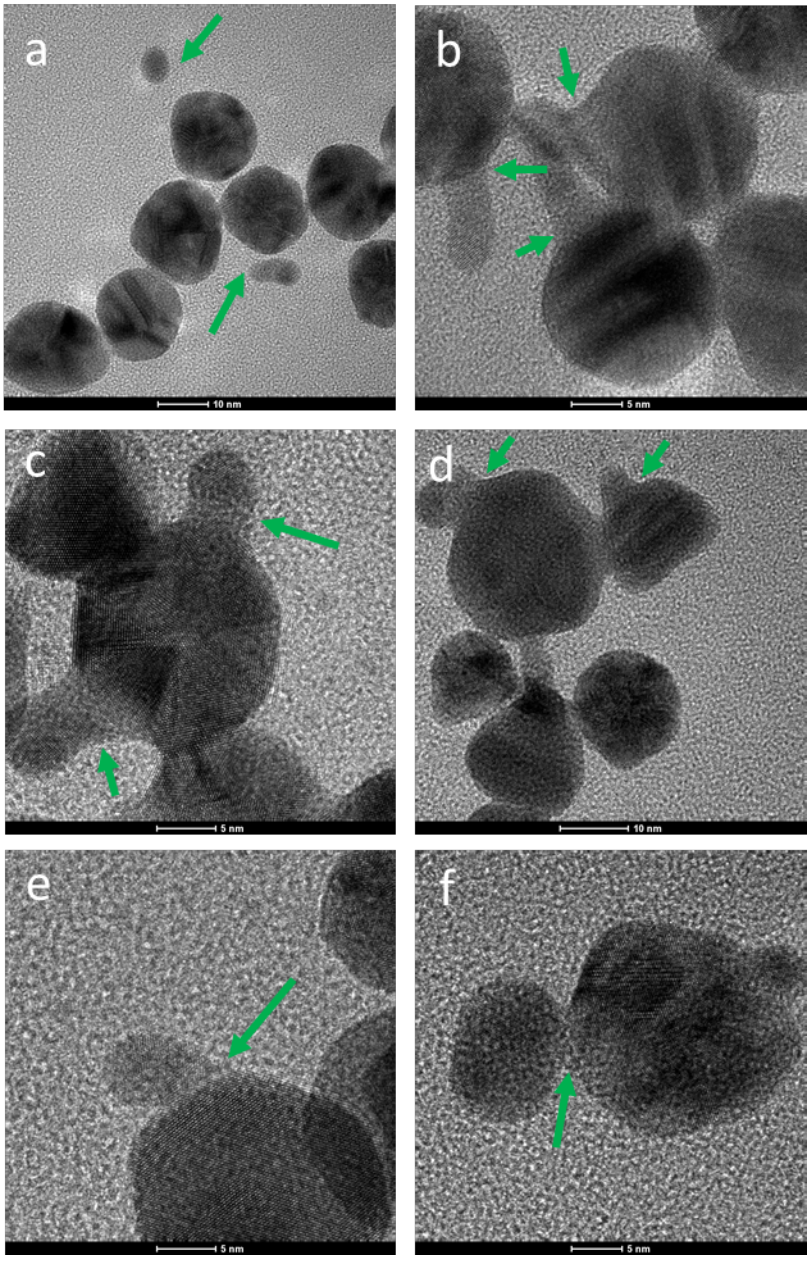

Figure S4. *High-resolution ex situ TEM images showing the structure of the necks, highlighted by arrows, formed between the primary and secondary particles. Scale bars are 5 nm*

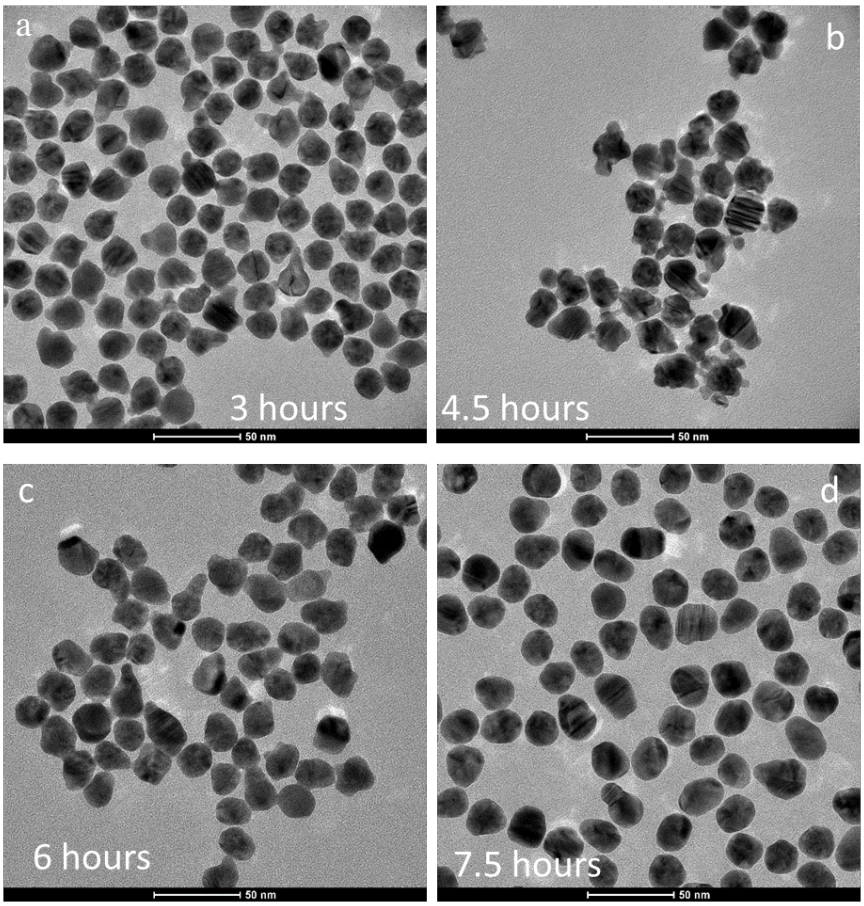

Figure S5. *Ex situ TEM images of the evolution of the seed crystals under neutral growth condition (pH 6.5). Scale bars are 50 nm*

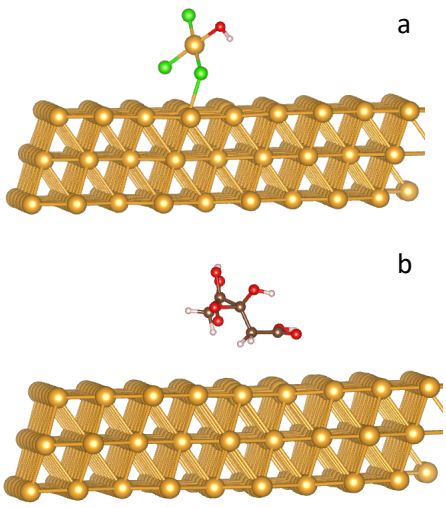

Figure S6. *Optimized configurations of precursor solution species on Au (111) surface. The dominant species at pH 6 are (a) $[AuCl_3OH]^-$ and (b) $[C_6H_6O_7]^{2-}$. Au atoms are shown as gold, O – as red, Cl – as green, C – as brown and H – as white spheres.*

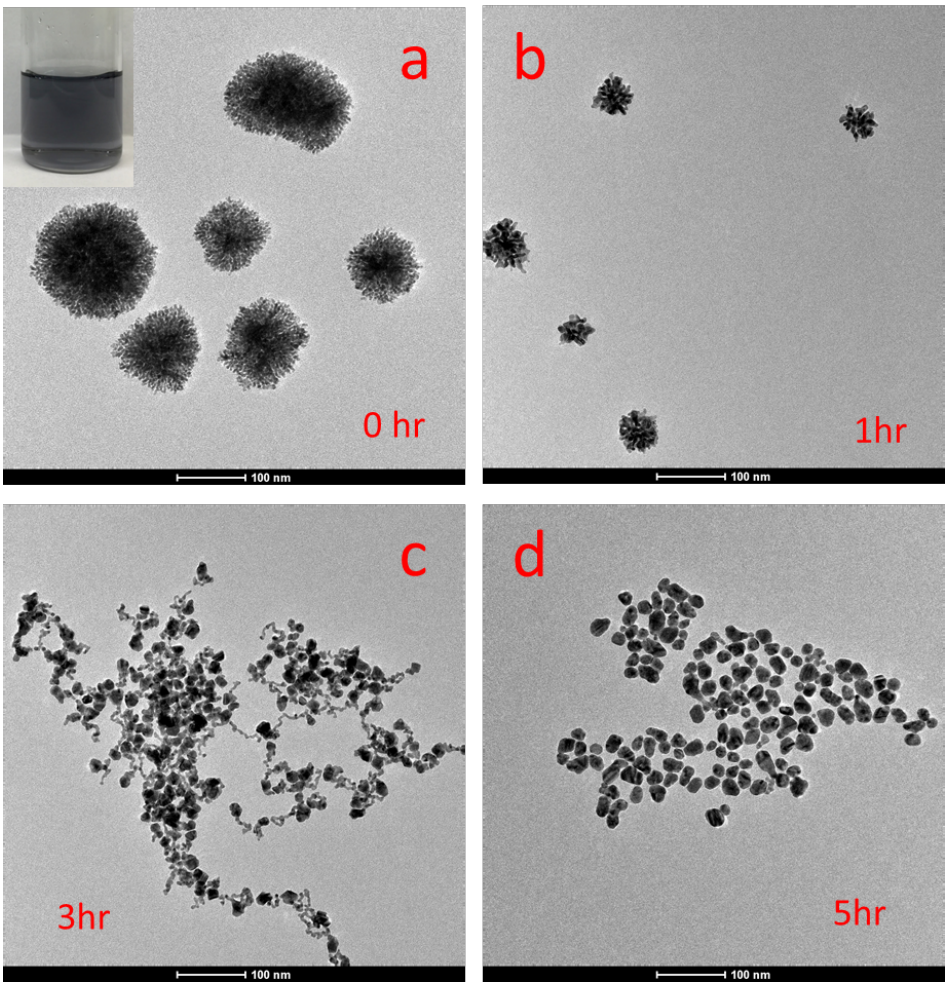

Figure S7. *Ex-situ TEM images of growth solution and evolution of the agglomerates without pre-existing seeds. The inset in (a) shows an image of the greyish color growth solution with agglomerates. Scale bars are 100 nm*

References

1. Turkevich, J.; Stevenson, P. C.; Hillier, J., A study of the nucleation and growth processes in the synthesis of colloidal gold. *Discussions of the Faraday Society* **1951,** *11*, 55.
2. Ji, X.; Yang, W., High-purity gold nanocrystal dimers: scalable synthesis and size-dependent plasmonic and Raman enhancement. *Chem. Sci.* **2014,** *5* (1), 311-323.
3. Park, J.-W.; Shumaker-Parry, J. S., Structural Study of Citrate Layers on Gold Nanoparticles: Role of Intermolecular Interactions in Stabilizing Nanoparticles. *Journal of the American Chemical Society* **2014,** *136* (5), 1907-1921.

4. Sandroff, C. J.; Herschbach, D. R., Kinetics of displacement and charge transfer reactions probed by SERS: evidence for distinct donor and acceptor sites on colloidal gold surfaces. *Langmuir : the ACS journal of surfaces and colloids* **1985,** *1* (1), 131-135.
5. Woehl, T. J.; Evans, J. E.; Arslan, L.; Ristenpart, W. D.; Browning, N. D., Direct in Situ Determination of the Mechanisms Controlling Nanoparticle Nucleation and Growth. *Acs Nano* **2012,** *6* (10), 8599-8610.
6. Chen, W.; Wang, H. T.; Li, Y. Z.; Liu, Y. Y.; Sun, J.; Lee, S. H.; Lee, J. S.; Cui, Y., In Situ Electrochemical Oxidation Tuning of Transition Metal Disulfides to Oxides for Enhanced Water Oxidation. *Acs Central Sci* **2015,** *1* (5), 244-251.
7. Zheng, H. M.; Claridge, S. A.; Minor, A. M.; Alivisatos, A. P.; Dahmen, U., Nanocrystal Diffusion in a Liquid Thin Film Observed by in Situ Transmission Electron Microscopy. *Nano Lett* **2009,** *9* (6), 2460-2465.
8. Woehl, T. J.; Jungjohann, K. L.; Evans, J. E.; Arslan, I.; Ristenpart, W. D.; Browning, N. D., Experimental procedures to mitigate electron beam induced artifacts during in situ fluid imaging of nanomaterials. *Ultramicroscopy* **2013,** *127*, 53-63.
9. Park, J. H.; Schneider, N. M.; Grogan, J. M.; Reuter, M. C.; Bau, H. H.; Kodambaka, S.; Ross, F. M., Control of Electron Beam-Induced Au Nanocrystal Growth Kinetics through Solution Chemistry. *Nano Lett* **2015,** *15* (8), 5314-5320.
10. Habraken, W. J. E. M.; Tao, J.; Brylka, L. J.; Friedrich, H.; Bertinetti, L.; Schenk, A. S.; Verch, A.; Dmitrovic, V.; Bomans, P. H. H.; Frederik, P. M.; Laven, J.; van der Schoot, P.; Aichmayer, B.; de With, G.; DeYoreo, J. J.; Sommerdijk, N. A. J. M., Ion-association complexes unite classical and non-classical theories for the biomimetic nucleation of calcium phosphate. *Nat Commun* **2013,** *4* (1507), 2490.
11. Sushko, M. L.; Rosso, K. M., The origin of facet selectivity and alignment in anatase TiO2 nanoparticles in electrolyte solutions: implications for oriented attachment in metal oxides. *Nanoscale* **2016,** *8* (47), 19714-19725.
12. Meng, D.; Zheng, B.; Lin, G.; Sushko, M. L., Numerical Solution of 3D Poisson-Nernst-Planck Equations Coupled with Classical Density Functional Theory for Modeling Ion and Electron Transport in a Confined Environment. *Commun Comput Phys* **2014,** *16* (5), 1298-1322.
13. Ojea-Jimenez, I.; Campanera, J. M., Molecular Modeling of the Reduction Mechanism in the Citrate Mediated Synthesis of Gold Nanoparticles. *J Phys Chem C* **2012,** *116* (44), 23682-23691.
14. Wright, L. B.; Rodger, P. M.; Walsh, T. R., Aqueous citrate: a first-principles and force-field molecular dynamics study. *Rsc Adv* **2013,** *3* (37), 16399-16409.
15. Zhu, C.; Liang, S. X.; Song, E. H.; Zhou, Y. J.; Wang, W.; Shan, F.; Shi, Y. T.; Hao, C.; Yin, K. B.; Zhang, T.; Liu, J. J.; Zheng, H. M.; Sun, L. T., In-situ liquid cell transmission electron microscopy investigation on oriented attachment of gold nanoparticles. *Nature Communications* **2018,** *9*, 421.
16. Ye, Q.; Zhou, J.; Zhao, T.; Zhao, H. F.; Chu, W. S.; Sheng, Z. X.; Chen, X.; Marcelli, A.; Luo, Y.; Wu, Z. Y., Identification of 13- and 14-Coordinated Structures of First Hydrated Shell of [AuCl4](-) Acid Aqueous Solution by Combination of MD and XANES. *J Phys Chem B* **2012,** *116* (27), 7866-7873.
17. Sushko, M. L.; Thomas, D. G.; Pabit, S. A.; Pollack, L.; Onufriev, A. V.; Baker, N. A., The Role of Correlation and Solvation in Ion Interactions with B-DNA. *Biophys J* **2016,** *110* (2), 315-326.
18. Sushko, M. L.; Rosso, K. M., Role of hydration forces in the properties of electrolyte solutions in the bulk and at interfaces. *MRS Online Proceedings Library* **2015,** *1753*, doi:10.1557/opl.2015.108.